IEEE Photonics Journal
An IEEE Photonics Society Publication

Open Access

Improving the Linearity of Silicon Ring Modulators by Manipulating the Photon Dynamics

Volume 12, Number 2, April 2020

Qiang Zhang
Hui Yu
Zhilei Fu
Xiaofei Wang
Penghui Xia
Qiman Cheng
Jianyi Yang

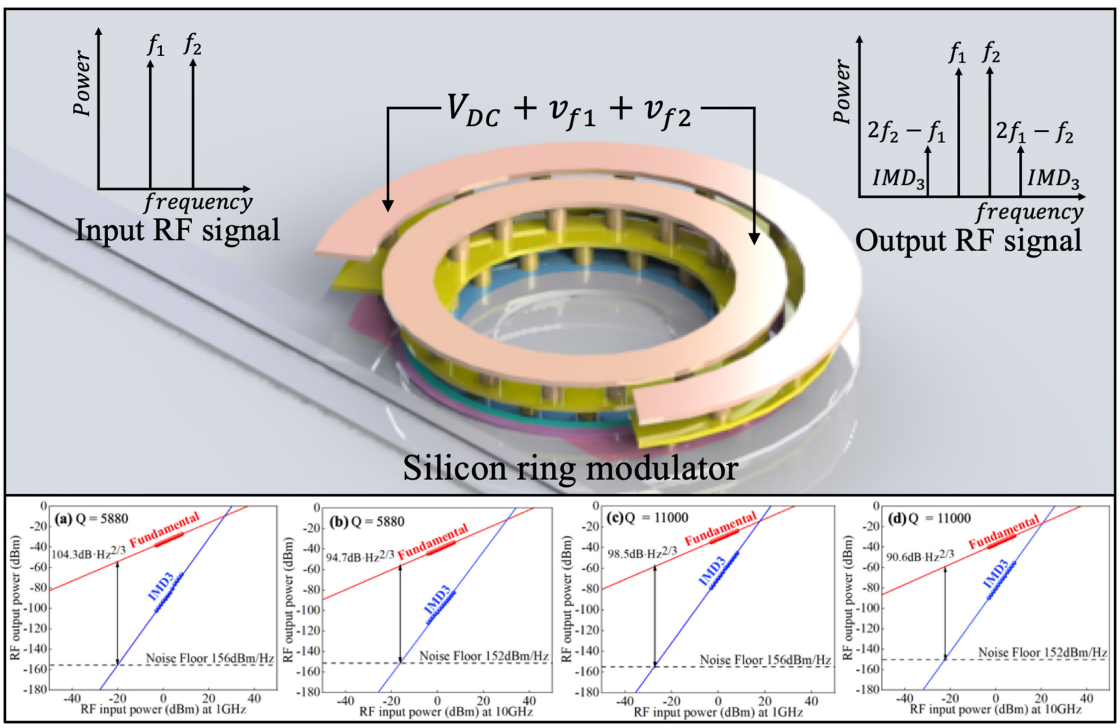

DOI: 10.1109/JPHOT.2020.2979917

Improving the Linearity of Silicon Ring Modulators by Manipulating the Photon Dynamics

Qiang Zhang, Hui Yu, Zhilei Fu, Xiaofei Wang, Penghui Xia, Qiman Cheng, and Jianyi Yang

Institute of Integrated Microelectronic Systems, College of Information Science and Electronic Engineering, Zhejiang University, Hangzhou 310027, China

DOI:10.1109/JPHOT.2020.2979917

Manuscript received January 4, 2020; revised March 5, 2020; accepted March 7, 2020. Date of publication March 10, 2020; date of current version March 24, 2020. This work was supported by the National Key R&D Program of China under Grant 2018YFB2200600. Corresponding author: Hui Yu (e-mail: huiyu@zju.edu.cn).

Abstract: We demonstrate that the linearity of silicon ring modulators can be improved significantly by manipulating the dynamics of photons in the cavity. A theoretically model is established to analyze the dependence of the modulation linearity on lifetime and wavelength of photons. By reducing *Q* factors of silicon ring modulators from 11000 to 5880 and tuning the operation wavelength, measured Spurious-Free Dynamic Ranges for the third-order intermodulation distortion are improved from 98.5 dB·Hz$^{2/3}$ to 104.3 dB·Hz$^{2/3}$ and from 90.6 dB·Hz$^{2/3}$ to 94.7 dB·Hz$^{2/3}$ at 1 GHz and 10 GHz, respectively.

Index Terms: Silicon nanophotonics, microwave photonics, microwave photonics signal processing.

1. Introduction

Microwave photonics (MWP) is a fast-developing field that studies the interaction between microwave and optical waves to realize generation, processing, control and distribution of microwave signals in the optical domain [1], [2]. Conventional MWP systems are usually composed of discrete fiber-optic components, and therefore suffer from bulky sizes and high sensitivities to external perturbations such as vibrations and temperature gradients [3], [4]. In order to solve these issues, the photonic integration technique is leveraged to implement on-chip MWP circuits on a variety of material systems, such as SiN [5]–[7], III-V compound semiconductor [8]–[10], silicon-on-insulator (SOI) [11]–[14], etc. Compared with other integration platforms, the MWP integration on SOI platform has many advantages, such as CMOS compatibility, high integration density, well-developed device library, and potential for seamless integration with electronics. As a result, it has received growing research attention [15], [16].

For an MWP link, a highly linear modulator is strongly demanded as it dominates the linearity of the entire link which is characterized quantitatively by the spurious free dynamic range (SFDR). Despite the MWP integration on SOI platform offers many advantages, it is challenging to achieve a silicon-based modulator with high linearity due to the lack of linear electro-optic (EO) effect on silicon [3]. Most all-silicon modulators therefore utilize the plasma dispersion effect by depleting free carriers in PN junction embedded rib waveguides with reverse bias voltages [17]–[19]. This

mechanism results in a nonlinear dependence of the effective index change on the driving voltage. However, a carrier-depletion-based silicon Mach-Zehnder modulator (MZM) can be linearized by choosing proper operation point and phase shifter length. The principle behind is that the nonlinearity of the PN junction cancels that of the cosine-squared transfer function of the MZM [20]. An alternative solution is to cascade dual MZMs in parallel or in series so that nonlinearities of the two sub-MZMs counteract each other [21]. With all these efforts, linearities of silicon carrier-depletion-based MZMs are improved to a level that is comparable with the $LiNbO_3$ modulator.

Another configuration widely used by the silicon photonics community is the silicon ring modulator [22]–[27]. Thanks to the resonance enhancement effect, ring modulators have significantly reduced driving voltages which are very prospective for improving the gain characteristics of MPW links. However, the modulation dynamics in a ring modulator is far more complex than that in an MZM [25]. Modulation linearities of silicon ring modulators are generally inferior to those of silicon MZMs, e.g., the SFDR of the all-silicon carrier-depletion-based ring modulator is measured to be 84 dB·Hz$^{2/3}$ in [24]. In order to linearize the silicon ring modulator, an x-cut ion-sliced $LiNbO_3$ membrane with linear EO effect is transferred to the top of a silicon ring resonator by the bonding technique in [28]. The resultant hybrid silicon-$LiNbO_3$ ring modulator presents SFDRs of 98.1 dB·Hz$^{2/3}$ and 87.6 dB·Hz$^{2/3}$ at 1 GHz and 10 GHz, respectively. Although the hybrid integration of EO materials could improve the modulation linearity significantly, the CMOS compatibility rises as an issue. Recently, the convex nonlinearity of the DC-Kerr effect is utilized to balance the concave nonlinearity of the carrier-depletion effect [29]. The interplay of the two effects inside a well-designed silicon PIN junction produces a nearly linear relationship between the effective index change and the driving voltage. A linear silicon ring modulator thus is demonstrated with a SFDR of 103.6 dB·Hz$^{2/3}$ at 1.2 GHz. To further increase the linearity, based on the previous work [29], the SFDR is improved to 108 dB·Hz$^{2/3}$ by the method of predistortion [30]. However, the cost is that its modulation efficiency degrades to 7 pm/V. In contrast, modulation efficiencies of most reported silicon ring modulators are well beyond 20 pm/V [31], [32]. Moreover, the predistortion method needs an external high-speed predistorter circuit, introducing more complexity to the link.

In this work, we develop a much simple and useful technique to improve the linearity of silicon ring modulators. With the intrinsic advantage of low driving-voltage, highly linear ring modulators can play an important role in integrated MWP systems on SOI platform. Specifically, we optimize the photon dynamics inside the silicon ring cavity by tuning the quality factor (*Q*-factor) and the operation wavelength for a high linearity modulation. The measured SFDRs for the third-order intermodulation distortion (IMD3) are as high as 104.3/94.7 dB·Hz$^{2/3}$ at 1/10 GHz with a silicon ring modulator whose *Q* factor is 5880. To the best of our knowledge, this result represents the highest linearity achieved with silicon ring modulators instead of complex signal processing such as predistortion.

The paper is organized as follows: At first, the principle of linearizing the silicon ring modulator by manipulating the photon dynamics is explained in Section 2. Subsequently, we design, fabricate and characterize two silicon ring modulators with different *Q* factors in Section 3. After that, the SFDRs of the two devices are characterized and compared by sweeping the operation wavelength at different frequencies. Finally, we reach a conclusion in Section 5.

2. Theoretical Basis of Linearization

It is known that the dynamic response of photons in a cavity is dominated by the *Q* factor of the cavity and the wavelength of photons [25]. Therefore, we analyze the linearity of the silicon ring modulator with the *Q* factor and the operation wavelength being variables in this section. The normalized transmission at the through port of a ring resonator can be represented by the normalized Lorentzian function *T(λ)* in Eq. (1) [33], [34]

$$T(\lambda) = 1 - \frac{A}{1 + 4\left[\frac{\lambda - \lambda_0 - \lambda_{shift}(v)}{\Delta\lambda}\right]^2} \tag{1}$$

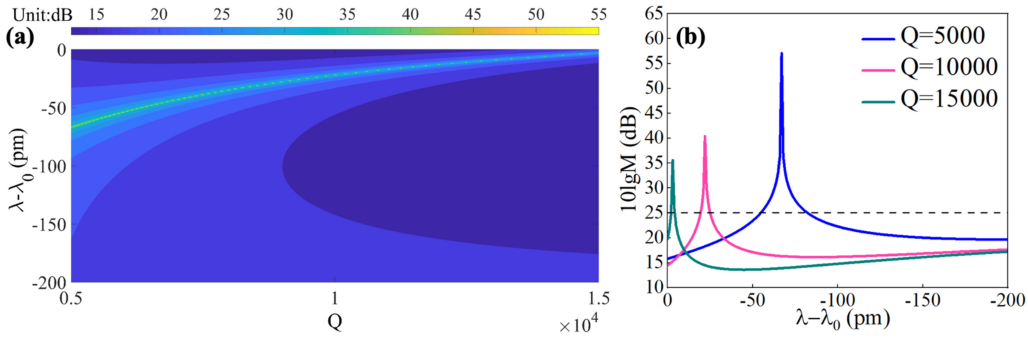

Fig. 1. (a) Contour map of 10lgM as a function of the Q factor and the operation wavelength. (b) The relationship between 10lgM and the operation wavelength at different Q values.

where A is a constant which determines the intrinsic extinction of the ring. The value of A equals to one if the ring is critical coupled. The Q factor of the ring is calculated as $\lambda_0/\Delta\lambda$, where λ_0 and $\Delta\lambda$ denote the central wavelength and the optical 3-dB bandwidth of the resonance curve respectively. For a silicon carrier-depletion-based ring modulator, the relationship between the resonance wavelength shift $\lambda_{\rm shift}(v)$ and the applied voltage v can be described by Eq. (2) [35].

$$\lambda_{\rm shift}(v) = \alpha\left(\sqrt{v+\beta} - \sqrt{\beta}\right) \tag{2}$$

The parameters α and β in Eq. (2) reflect the modulation efficiency of the practical device. Their values can be extracted from measured resonance spectra by data fitting. The plasma dispersion effect changes both refractive index and absorption coefficient of silicon. However, for simplicity, we do not consider the variation of waveguide propagation loss during the modulation. It implies that the value of A is a constant. Substituting Eq. (2) into Eq. (1) yields the transmitted optical power at different bias voltages. By calculating the voltage-induced change in the transmitted optical power, we deduce the modulation transfer function in Eq. (3)

$$I(v) = 1 - \frac{A\lambda_0^2}{\lambda_0^2 + 4Q^2\left[(\lambda-\lambda_0) + \alpha\sqrt{\beta} - \alpha\sqrt{v+\beta}\right]^2} \tag{3}$$

The intensity modulation in Eq. (3) depends on both operation wavelength λ and Q factor. According to the nonlinear modulation theory [21], amplitudes of the first harmonic (FH) and the IMD3 components in the modulated optical field are $I'(V_{\rm DC})v_0$ and $I'''(V_{\rm DC})v_0{}^3/8$ and $I'''(V_{\rm DC})v_0{}^3/8$, respectively, in the small signal regime. Here, $V_{\rm DC}$ and v_0 denote the DC bias point and the amplitude of driving AC signal, respectively. The parameter $M = 8I'(V_{\rm DC})/I'''(V_{\rm DC})$ denotes the relative amplitude of the FH component with respect to the IMD3 component when $v_0 = 1$ V. It therefore can be utilized to evaluate the linearity of the ring modulator approximately. A widely used performance metric to reflect the modulation linearity is the carrier-to-distortion ratio (CDR) which varies with v_0 [20]. Therefore, the parameter M is actually equivalent to the CDR/2 at the certain driving level of $v_0 = 1$ V. A large M implies a weak IMD3 component relative to the FH component, and hence a high linearity.

In Fig. 1(a), we calculate 10lg(M) as a function of Q factor and $\lambda-\lambda_0$ at a reverse bias voltage of -2 V. Values of α, β and A in our calculation are 0.09, 3.5 and 0.997, respectively. These values are acquired from measured resonance spectrum shifts of practical ring modulators as will be presented in Section 3. It is apparent in Fig. 1(a) that as long as the value of Q is fixed, an optimal wavelength can be found to produce the highest modulation linearity. As the value of Q decreases, this optimal wavelength would gradually shift away from the resonance central wavelength. As elucidated in Fig. 1(b), a low-Q ring modulator exhibits a better linearity than a high-Q ring modulator when both devices operate near their optimal wavelengths. More importantly, the

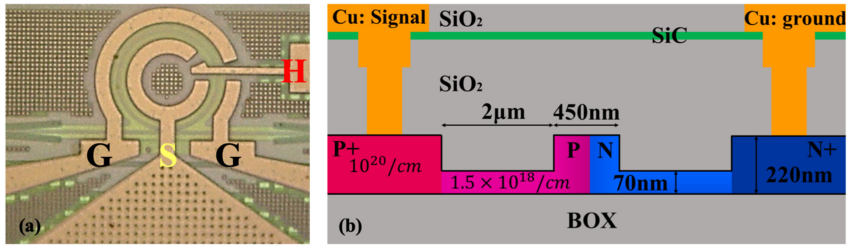

Fig. 2. (a) Microscope image of the ring modulator, G: ground; S: signal; H: heater. (b) Cross-sectional view of the PN junction of the ring modulator.

wavelength span to support a high modulation linearity becomes wider as the value of Q decreases. For example, wavelength ranges where M>25 dB in Fig. 1(b) are 28 nm and 2 nm for $Q = 5000$ and $Q = 15000$, respectively.

3. Measurement of DC and Dynamic Modulation Characteristics

Two silicon ring modulators with different Q factors are fabricated by joining the silicon photonics multi-project wafer (MPW) service of IMEC (ISIPP50G). Detailed descriptions of the processing platform can be found in [31]. Ring modulators are composed of rib waveguides which are incorporated with identical PN junctions. Dimension and etching depth of rib waveguides are 450 nm $\times$ 220 nm and 150 nm, respectively, while the radii of the two rings are 7 μm. The nominal doping concentration of the PN junctions is 1.5 $\times$ 10^{18}/cm^3. The ohmic contact regions are heavily doped to 10^{20}/cm^3 to reduce the contact resistance. They are optically isolated from the guided optical mode by 2-μm-wide trenches. In order to obtain different Q factors, the two devices have different gaps between bus waveguides and rings, which are 180 nm and 360 nm. The modulation areas where PN junctions are buried take up 70% of the overall perimeters of the two rings, while the rest parts of the two rings are uniformly doped to act as waveguide heaters. Fiber grating couplers interface the two devices with single mode fibers at their input and output ports. Microscope image and cross-sectional schematic diagram of one device are shown in Figs. 2(a) and 2(b), respectively.

After normalizing the insertion loss of the two fiber grating couplers, we plot measured transmission spectra of the two devices at different reverse bias voltages in Figs. 3(a) and 3(c). From the measured spectra, we can extract the Q factors and the resonance wavelength shifts of the two rings. Results then are displayed in Figs. 3(b) and 3(d) as a function of V_{DC}. At -1 V bias voltage, the two devices present similar modulation efficiencies of $\sim$20 pm/V. As the reverse bias voltage increases, free carriers that causing strong optical absorption are depleted. Owing to reduced round trip losses, Q factors of the two rings increase with the reverse bias voltage as shown in Figs. 3(b) and 3(d). The parameters α, β and A can be determined easily by using formulas in Eqs. (1)–(3) to fit curves in Figs. 3(a)–(d). Their values are $\alpha = 0.09$, $\beta = 3.5$ and $A = 0.997$ for the low-Q ring modulator, and $\alpha = 0.078$, $\beta = 3.5$ and $A = 0.93$ for the high-Q ring modulator.

Dynamic performances of the two devices are characterized by measuring their small-signal frequency responses with a light-wave component analyzer (LCA Keysight N4373D). The RF output power of the LCA is 0 dBm ($v_{\mathrm{pp}} = 0.63$ V) for the small-signal frequency response measurement. It is known that the dynamic response of a silicon ring modulator relies on the operation wavelength [25]. In order to make a fair comparison, operation wavelengths of both devices are tuned carefully to maximize the strength of the S21 parameter before we measure the bandwidth. Measured EE-S21 parameters are displayed in Fig. 4, where electrical 3 dB modulation bandwidths of the low Q and the high Q ring modulators are 33 GHz and 11 GHz, respectively.

If the wavelength dependence is not considered, an empirical formula to simply estimate the 3 dB bandwidth of a ring modulator is $1/{f_{3\mathrm{dB}}}^2 = 1/{f_{\mathrm{Q}}}^2 + 1/{f_{\mathrm{RC}}}^2$. Here f_{Q} and f_{RC} are the bandwidth limitations imposed by the photon lifetime and the RC time constant, respectively. Since the

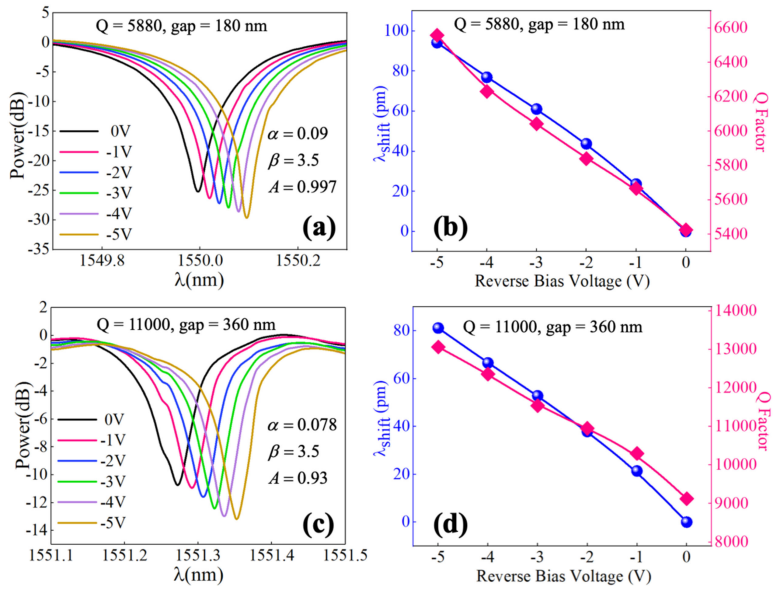

Fig. 3. (a) and (c) Measured transmission spectra of the two ring modulators at different reverse bias voltages. (b) and (d) Resonance wavelength shifts and Q factors of the two rings vs. the reverse bias voltage.

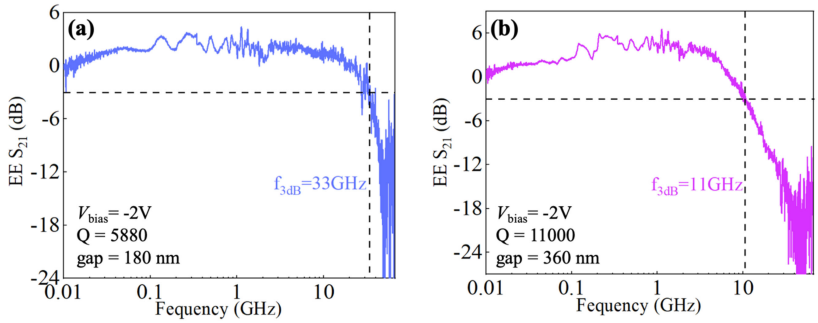

Fig. 4. Measured small signal frequency responses of two devices at a reverse bias voltage of -2 V. (a) $Q = 5880$ and (b) $Q = 11000$.

two devices differ only in their coupling gaps, their RC time constants are identical in principle. According to the PDK document released by imec, the RC time constant limited 3 dB bandwidth is more than 50 GHz thanks to compact footprints of the two rings. It is far higher than the measured bandwidths in Fig. 4. On the other hand, photon lifetime limited 3 dB bandwidths of the two devices are 33 GHz and 17 GHz according to the formula $f_{\mathrm{Q}} = c/(Q\lambda_0)$, which are very close to the measurement results in Fig. 4. Therefore, the photon lifetime is the major limiting factor of modulation bandwidth. Thanks to its short cavity photon lifetime, the low Q ring has a much higher bandwidth than the high Q ring modulator.

4. Measurement of the Modulation Linearity

In order to verify the theoretical analysis in Section 2, the two-tone test is implemented to characterize SFDRs of the two devices. The measurement setup is shown in Fig. 5. TE polarized light from a continuous wave (CW) tunable laser (Santec TSL-710) is coupled into the modulator by the fiber grating coupler. The driving two-tone signal is generated by a RF source (Keysight

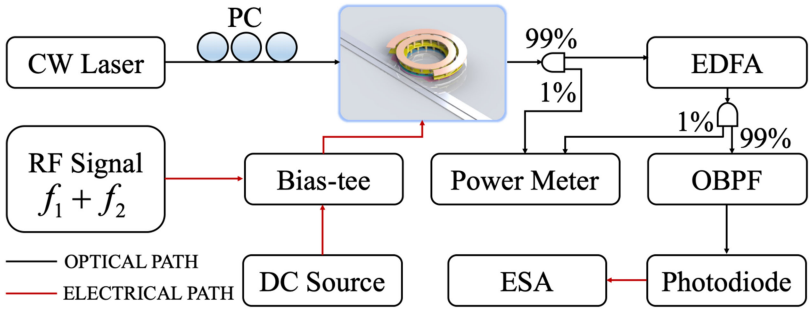

Fig. 5. Setup for the SFDR measurement. CW Laser: continuous wave tunable laser; EDFA: erbium doped fiber amplifier; OBPF: optical bandpass filter; ESA: electrical spectrum analyzer; and PC: polarization controller.

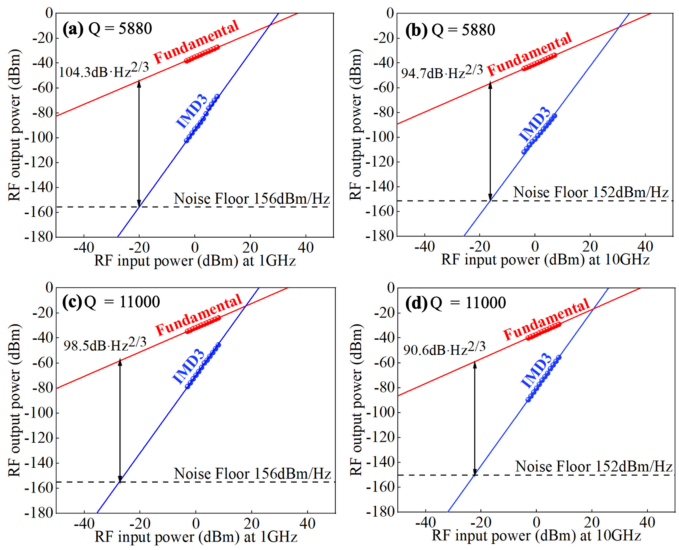

Fig. 6. Measured SFDRs of the two ring modulators at different modulation frequencies. (a) $Q = 5880$ at 1 GHz, (b) $Q = 5880$ at 10 GHz, (c) $Q = 11000$ at 1 GHz, and (d) $Q = 11000$ at 10 GHz.

E8267D). It is combined with a DC bias voltage before being fed to the modulator by a 50 GHz RF probe. The output of the modulator is amplified by an erbium doped fiber amplifier (EDFA) (Amonics AEDFA-PA-35-B-FA) so as to compensate the ~8 dB coupling loss of the two fiber grating couplers and the insertion loss of the device itself. An optical bandpass filter (OBPF WaveShaper 2000A) is used to suppress the amplified spontaneous emission noise (ASE) of the EDFA. The optical-to-electrical conversion is performed by a 30 GHz photodiode with a responsivity of 0.75 A/W. The output RF signal of the PD is analyzed by a 67 GHz electrical spectrum analyzer (ROHDE&SCHWARZ FSWP). During the measurement, the amplification rate of the EDFA is maintained at 18 dB. As shown in Fig. 5, two 1/99 power splitters and a two-channel optical power meter are used to monitor the amplification ratio. The two tones with a spacing of 10 kHz are centered at 1 GHz or 10 GHz in the measurement. The noise floors measured by the spectrum analyzer are 156 dBm/Hz and 152 dBm/Hz when frequency centers of the two tones locates at 1 GHz and 10 GHz, respectively. The higher noise floor at high RF frequency is mainly due to the signal source and the ESA which are frequency dependent.

As analyzed in Section 2, the linearity of a ring modulator depends on the operation wavelength. Therefore, the SFDRs of the two devices are measured by sweeping the wavelength of the laser. In Fig. 6, SFDRs of the two devices are compared while both of them operate at their optimal

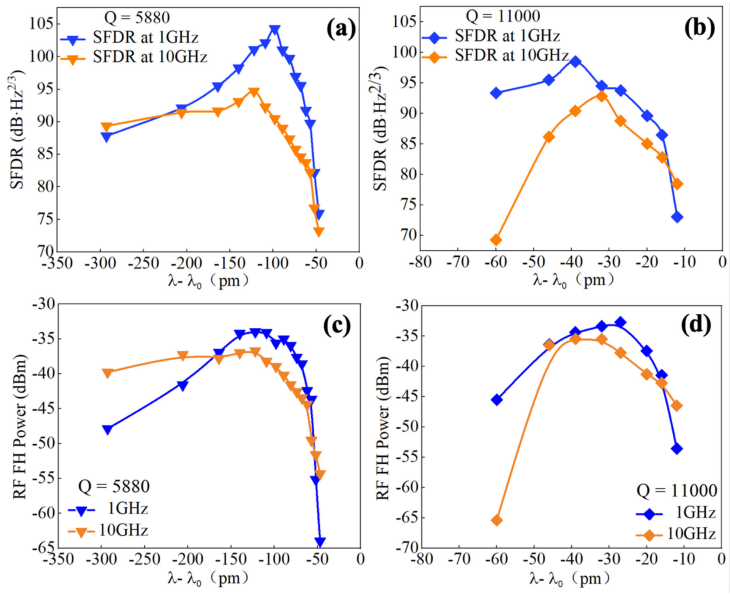

Fig. 7. The relationship between the SFDR and the operation wavelength λ–λ_0 of (a) $Q = 5880$ and (b) $Q = 11000$. The relationship between the power of FH component and the operation wavelength λ–λ_0 of (c) $Q = 5880$ and (d) $Q = 11000$.

wavelengths with the highest modulation linearities. It can be seen that as the Q factor decreases from 11000 to 5880, SFDRs are improved by 5.8 dB·Hz$^{2/3}$ and 4.1 dB·Hz$^{2/3}$ at 1 GHz and 10 GHz, respectively.

To find the dependence of the modulation linearity of the ring on the operation wavelength, we plot SFDRs of the two devices as a function of $\lambda-\lambda_0$ in Figs. 7(a) and 7(b). It should be noted that the exact resonance central wavelength λ_0 of the ring resonator is uncertain during the SFDR measurement. The reason is that the local temperature of the ring varies with the power of the driving RF signal due to the accompanying heating effect. Therefore, we infer the approximate value of $\lambda-\lambda_0$ according to the average optical power probed by the power monitor in the link and the resonance spectra in Fig. 3. At 1 GHz, the measured optimal linear operation wavelengths are $\sim$100 pm and $\sim$38 pm away from the resonance central wavelengths for $Q =$ 5880 and $Q =$ 11000, respectively. Here the optimal linear operation wavelength is defined as the wavelength with the highest SFDR. In contrast, the calculated optimal wavelength detunings from the resonance central wavelengths in Fig. 1(a) are 60 pm for $Q = 5880$, and 20 pm for $Q =$ 11000. The deviations between measurement and calculation can be attributed to the imprecise estimation of $\lambda-\lambda_0$ according to the average power of the modulated optical signal. The SFDRs in Figs. 7(a) and 7(b) deteriorate as the frequency rises from 1 GHz to 10 GHz. This phenomenon is universal for SFDR measurements [28] due to the reason that signal-to-noise ratios of any links always drop at high operation frequencies. In addition, modulation depths of any modulators also drop with increasing the frequency, so powers of FH components at 10 GHz are weaker than those at 1 GHz in Figs. 7(c) and 7(d).

In Figs. 7(a) and 7(b), the peak SFDRs of the low Q ring (104.3/94.7 dB·Hz$^{2/3}$ at 1/10 GHz) are higher than those of the high Q ring (98.5/90.6 dB·Hz$^{2/3}$ at 1/10 GHz). Moreover, the low Q ring present a much wider linear operation wavelength range than the high Q ring. Here the linear operation wavelength range is defined as the wavelength span in which the SFDR is higher than 95 dB·Hz$^{2/3}$ at 1 GHz. Its values are 100 pm and 16 pm for the low Q and the high Q rings, respectively. Therefore, reducing the Q factor indeed improves the modulation linearity of the ring. However, on the other hand, it suppresses the sensitive of the ring to the refractive index modulation and then weaken the optical modulation amplitude. It is hence necessary to examine

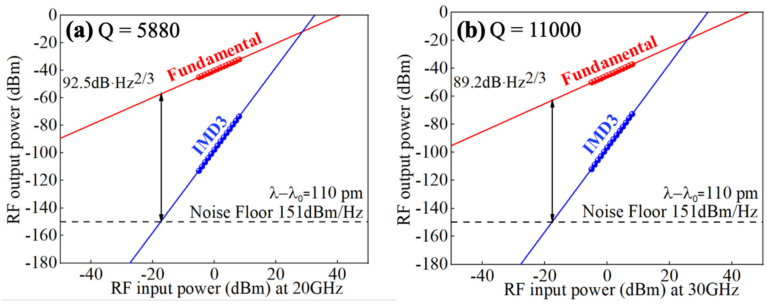

Fig. 8. Measured SFDRs of the ring modulators ($Q = 5880$) at different modulation frequencies. (a) at 20 GHz and (b) at 30 GHz.

TABLE 1
A Comparison of Our Device With the State of the Art

	Linearization technique	Q	Modulation efficiency (pm/V)	EE S21 (GHz)	SFDR (dB·Hz$^{2/3}$) at 1/10/20/30 GHz
A. Ayazi [24]	\	5000	10.6	18.8	84/None/None/None
L. Chen [28]	Bonding LiNbO3 membrane	14400	5.3	15	98.1/87.6/None/None
A. Jain [29]	Employing the DC Kerr effect	17000	7	4.47	103.6/None/None/None
A. Jain [30]	DC Kerr effect and predistortion	15570	2	13.3	108/ None/None/None
Our work	Tuning the photon dynamics	5880	19	33	104.3/94.7/92.5/89.2

the penalty to the FH component when we linearize the ring modulator. In Figs. 7(c) and 7(d), we plot the power of the FH component versus the operation wavelength for the two devices. When operating at wavelengths with maximum SFDRs, the low-Q ring modulator of $Q = 5880$ generates FH components of -35.6 dBm and -36.7 dBm at 1 GHz and 10 GHz, respectively. In contrast, the high-Q ring modulator of $Q = 11000$ generates FH components of -34.4 dBm and -35.5 dBm at 1 GHz and 10 GHz, respectively. Therefore, the power penalty to the FH component is $\sim$1.2 dB when the ring modulator is linearized by reducing the Q factor.

We note that almost all linearity measurements of ring modulators are performed at frequencies lower than 10 GHz [24], [28]–[30]. However, for many wideband MWP systems, frequencies of RF signals can reach dozens of Gigahertz. Thus, it is very necessary to characterize the linearity of the silicon ring modulator at higher frequencies. In Fig. 8, SFDRs of the low Q ring modulator are measured to be 92.5 dB·Hz$^{2/3}$ and 89.2 dB·Hz$^{2/3}$ at 20 GHz and 30 GHz, respectively. The two measurements here are implemented with the two devices operating at the optimal wavelengths for high linearity modulation. Exact operation wavelengths are labeled inside Fig. 8. The relative intensity noise (RIN) of our tunable laser is -145 dB/Hz. We believe that if a laser with lower RIN noise is utilized to suppress the noise floor, the measured SFDR then can be improve significantly. For example, the SFDR would increase about 3 dB if the RIN of the input laser decrease 5 dB.

5. Conclusion

The device in this work is compared favorably with published highly linear silicon ring modulators in Table 1. It can be seen that manipulating the dynamics of photons by optimizing operation wavelength and Q factor is a simply effective way to improve the linearity of the ring modulator. Ring modulators in [28] and [29] utilize modulation effects which have much better linearity than

the carrier depletion effect we used in this paper. However, ultimate SFDRs in [28] and [29] are inferior to our device as a result of their high Q factors. Though the ring modulator in [30] utilizes the predistortion to further improve the linearity, it needs a complex external predistortion circuit whose bandwidth requires higher than the highest harmonic generated by the predistorter. We want to stress that different linearization techniques in Table. 1 can be combined so as to generate a silicon ring modulator with ultrahigh linearity.

In conclusion, we systematically characterize and compare linearities of two silicon ring modulators with different Q factors by sweeping the operation wavelength. A theoretical model is provided to explain the comparison result. Specifically, we demonstrate a highly linear silicon ring modulator whose SFDR for the IMD3 is 104.3/94.7/92.5/89.2 dB·Hz$^{2/3}$ at 1/10/20/30 GHz by reducing the Q factor and choosing proper operation wavelength. This work proves that the linearity of silicon ring modulators can be improved substantially by manipulating the photon dynamics. Compared with previously reported high linearity silicon ring modulators, this technique is easy to implement with no additional processing development cost, and is helpful to build high-performance MWP links based on silicon ring modulators. For example, feedback control systems similar to those in [36], [37] can be easily established with the average optical power as the feedback signal, then the resonance wavelength can be tuned by the heater and locked at the optimal offset position with respect to the lasing wavelength. Our theoretical calculation suggests that SFDRs higher than 110 dB·Hz$^{2/3}$ can be achieved with Q factors less than 4000. However, this benefit in modulation linearity comes at the expense of degraded modulation depth and link gain.

Acknowledgment

The authors would like to thank Dr. Bing Wei, Training Platform of Information and Microelectronic Engineering in Polytechnic Institute of Zhejiang University.

References

[1] J. Capmany and D. Novak, "Microwave photonics combines two worlds," *Nat. Photonics*, vol. 1, no. 6, pp. 319–330, 2007.
[2] J. Yao, "Microwave photonics," *J. Lightwave Technol.*, vol. 27, no. 3, pp. 314–335, 2009.
[3] D. Marpaung, C. Roeloffzen, R. Heideman, A. Leinse, S. Sales, and J. Capmany, "Integrated microwave photonics," *Laser Photon. Rev.*, vol. 7, no. 4, pp. 506–538, 2013.
[4] D. Marpaung, J. Yao, and J. Capmany, "Integrated microwave photonics," *Nat. Photonics*, vol. 13, no. 2, pp. 80–90, 2019.
[5] C. G. H. Roeloffzen *et al.*, "Silicon nitride microwave photonic circuits," *Opt. Express*, vol. 21, no. 19, pp. 22937–22961, 2013.
[6] Y. Xie, L. Zhuang, and A. J. Lowery, "Picosecond optical pulse processing using a terahertz-bandwidth reconfigurable photonic integrated circuit," *Nanophotonics*, vol. 7, no. 5, pp. 837–852, 2018.
[7] L. Zhuang, C. G. H. Roeloffzen, M. Hoekman, K. Boller, and A. J. Lowery, "Programmable photonic signal processor chip for radiofrequency applications," *Optica*, vol. 2, no. 10, pp. 854–859, 2015.
[8] J. S. Fandiño, P. Muñoz, D. Doménech, and J. Capmany, "A monolithic integrated photonic microwave filter," *Nat. Photon.*, vol. 11, no. 2, pp. 124–129, 2017.
[9] W. Liu *et al.*, "A fully reconfigurable photonic integrated signal processor," *Nat. Photon.*, vol. 10, no. 3, pp. 190–195, 2016.
[10] N. Andriolli, P. Velha, M. Chiesa, A. Trifiletti, and G. Contestabile, "A directly modulated multiwavelength transmitter monolithically integrated on InP," *IEEE J. Sel. Top. Quantum Electron.*, vol. 24, no. 1, pp. 1–6, Jan.–Feb. 2017.
[11] A. Ribeiro, A. Ruocco, L. Vanacker, and W. Bogaerts, "Demonstration of a 4 × 4-port universal linear circuit," *Optica*, vol. 3, no. 12, pp. 1348–1357, 2016.
[12] D. Pérez *et al.*, "Multipurpose silicon photonics signal processor core," *Nat. Commun.*, vol. 8, no. 1, pp. 636–644, 2017.
[13] W. Zhang and J. Yao, "Silicon-based integrated microwave photonics," *IEEE J. Quantum Electron.*, vol. 52, no. 1, pp. 1–12, 2015.
[14] M. H. Khan *et al.*, "Ultrabroad-bandwidth arbitrary radiofrequency waveform generation with a silicon photonic chip-based spectral shaper," *Nat. Photon.*, vol. 4, no. 2, pp. 117–122, 2010.
[15] L. R. Chen, "Silicon photonics for microwave photonics applications," *J. Lightw. Technol.*, vol. 35, no. 4, pp. 824–835, Feb. 2018.
[16] J. S. Orcutt *et al.*, "Open foundry platform for high-performance electronic-photonic integration," *Opt. Express*, vol. 20, no. 11, pp. 12222–12232, 2012.
[17] G. T. Reed, G. Mashanovich, F. Y. Gardes, and D. J. Thomson, "Silicon optical modulators," *Nat. Photon.*, vol. 4, no. 8, pp. 518–526, 2010.

[18] E. Timurdogan, C. M. Sorace-Agaskar, J. Sun, E. S. Hosseini, A. Biberman, and M. R. Watts, "An ultralow power athermal silicon modulator," *Nat. Commun.*, vol. 5, 2014, Art. no. 4008.
[19] A. Samani *et al.*, "Experimental parametric study of 128 Gb/s PAM-4 transmission system using a multi-electrode silicon photonic Mach Zehnder modulator," *Opt. Express*, vol. 25, no. 12, pp. 13252–13262, 2017.
[20] A. M. Gutierrez *et al.*, "Analytical model for calculating the nonlinear distortion in silicon-based electro-optic distortion in silicon-based electro-optic," *J. Lightw. Technol.*, vol. 31, no. 23, pp. 3603–3613, Dec. 2013.
[21] Q. Zhang *et al.*, "Linearity comparison of silicon carrier-depletion-based single, dual-parallel, and dual-series Mach–Zehnder modulators," *J. Lightw. Technol.*, vol. 36, no. 16, pp. 3318–3331, Aug. 2018.
[22] S. Manipatruni, L. Chen, and M. Lipson, "Ultra high bandwidth WDM using silicon microring modulators," *Opt. Express*, vol. 18, no. 16, pp. 16858–16867, 2010.
[23] P. Dong *et al.*, "Wavelength-tunable silicon microring modulator," *Opt. Express*, vol. 18, no. 11, pp. 10941–10946, 2010.
[24] A. Ayazi, T. Baehr-Jones, Y. Liu, A. E. Lim, and M. Hochberg, "Linearity of silicon ring modulators for analog optical links," *Opt. Express*, vol. 20, no. 12, pp. 13115–13122, 2012.
[25] H. Yu *et al.*, "Trade-off between optical modulation amplitude and modulation bandwidth of silicon micro-ring modulators," *Opt. Express*, vol. 22, no. 12, pp. 15178–15189, 2014.
[26] H. Yu *et al.*, "Silicon dual-ring modulator driven by differential signal," *Opt. Lett.*, vol. 39, no. 22, pp. 6379–6382, 2014.
[27] H. Shao *et al.*, "On-chip microwave signal generation based on a silicon microring modulator," *Opt. Lett.*, vol. 40, no. 14, pp. 3360–3363, 2015.
[28] L. Chen, J. Chen, J. Nagy, and R. M. Reano, "Highly linear ring modulator from hybrid silicon and lithium niobate," *Opt. Express*, vol. 23, no. 10, pp. 13255–13264, 2015.
[29] A. Jain, X. Wu, J. E. Bowers, R. Helkey, and J. Buckwalter, "Linear ring modulators with DC Kerr phase shifters," in *Proc. IEEE Avionics Vehicle Fiber-Opt. Photon. Conf.*, 2018, pp. 1–2.
[30] A. Jain *et al.*, "A high spur-free dynamic range silicon DC Kerr ring modulator for RF applications," *J. Lightw. Technol.*, vol. 37, no. 13, pp. 3261–3272, Jul. 2019.
[31] M. Pantouvaki *et al.*, "50 Gb/s silicon photonics platform for short-reach optical interconnects," in *Proc. Opt. Fiber Commun. Conf.*, 2016, Paper.Th4H.
[32] M. Pantouvaki *et al.*, "Active components for 50 Gb/s NRZ-OOK optical interconnects in a silicon photonics platform," *J. Lightw. Technol.*, vol. 35, no. 4, pp. 631–638, Feb. 2017.
[33] J. F. Buckwalter, X. Zheng, G. Li, K. Raj, and A. V. Krishnamoorthy, "A monolithic 25-Gb/s transceiver with photonic ring modulators and Ge detectors in a 130-nm CMOS SOI process," *IEEE J. Solid–State Circuits*, vol. 47, no. 6, pp. 1309–1322, Jun. 2012.
[34] C. Sun *et al.*, "A 45 nm CMOS-SOI monolithic photonics platform with bit-statistics-based resonant microring thermal tuning," *IEEE J. Solid–State Circuits*, vol. 51, no. 4, pp. 893–907, Apr. 2016.
[35] S. Moazeni, S. Lin, M. Wade, L. Alloatti, R. J. Ram, M. Popović, V. Stojanović, "A 40-Gb/s PAM-4 transmitter based on a ring-resonator optical DAC in 45-nm SOI CMOS," *IEEE J. Solid–State Circuits*, vol. 52, no. 12, pp. 3503–3516, 2017.
[36] X. Zheng *et al.*, "A high-speed, tunable silicon photonic ring modulator integrated with ultra-efficient active wavelength control," *Opt. Express*, vol. 22, no. 10, pp. 12628–12633, 2014.
[37] S. Lin *et al.*, "Wavelength locked high-speed microring modulator using an integrated balanced homodyne CMOS control circuit," in *Proc. Opt. Fiber Commun. Conf.*, 2016, Paper Th3J4.